Radiat Environ Biophys (2013) 52:397–410
DOI 10.1007/s00411-013-0471-z

ORIGINAL PAPER

Direct action of radiation on mummified cells: modeling of computed tomography by Monte Carlo algorithms

Johann Wanek · Robert Speller · Frank Jakobus Rühli

Received: 10 December 2012 / Accepted: 14 April 2013 / Published online: 25 April 2013

Abstract X-ray imaging is a nondestructive and preferred method in paleopathology to reconstruct the history of ancient diseases. Sophisticated imaging technologies such as computed tomography (CT) have become common for the investigation of skeletal disorders in human remains. Researchers have investigated the impact of ionizing radiation on living cells, but never on ancient cells in dry tissue. The effects of CT exposure on ancient cells have not been examined in the past and may be important for subsequent genetic analysis. To remedy this shortcoming, we developed different Monte Carlo models to simulate X-ray irradiation on ancient cells. Effects of mummification were considered by using two sizes of cells and three different phantom tissues, which enclosed the investigated cell cluster. This cluster was positioned at the isocenter of a CT scanner model, where the cell hit probabilities $P(0,1,\ldots, n)$ were calculated according to the Poisson distribution. To study the impact of the dominant physics process, CT scans for X-ray spectra of 80 and 120 kVp were simulated. Comparison between normal and dry tissue phantoms revealed that the probability of unaffected cells increased by 21 % following cell shrinkage for 80 kVp, while for 120 kVp, a further increase of unaffected cells of 23 % was observed. Consequently, cell shrinkage caused by dehydration decreased the impact of X-ray radiation on mummified cells significantly. Moreover, backscattered electrons in cortical bone protected deeper-lying ancient cells from radiation damage at 80 kVp X-rays.

Keywords CT imaging · Target theory · Cell shrinkage · Monte Carlo simulation · Ancient DNA

J. Wanek (✉) · F. J. Rühli
Centre for Evolutionary Medicine, Institute of Anatomy, University of Zürich, Winterthurerstrasse 190, 8057 Zurich, Switzerland
e-mail: johann.wanek@anatom.uzh.ch

J. Wanek · R. Speller
Department of Medical Physics and Bioengineering, University College London, Malet Place Engineering Building, Gower Street, London WC1E 6BT, UK

Introduction

What is a mummy? According to Lynnerup, mummies are human remains with preservation of soft tissue (Lynnerup 2007). Physical anthropology distinguishes between natural and artificial mummies. The natural or so-called spontaneous preservation of nonbony tissue takes place postmortem, usually under dry and cold (or hot) environmental conditions. A prominent subject of such mummification is the 5,300-year-old Iceman Oetzi, found in September 1991 in the Oetztal Alps. Spontaneous mummification is characterized through the rapid desiccation and preservation of visceral organs (Aufderheide et al. 2004). Note, however, that not all organs have the same preservation status; the spleen, for instance, often decays completely, whereas the lung is commonly preserved (Aufderheide et al. 2004).

Artificial mummification is characterized through active human intervention as practiced in many cultures with burial rites (Lynnerup 2007). Aufderheide called it anthropogenic mummification, where the purpose was to enhance royal authority by the early dynastic period (3,100–2,686 BC) in Egypt or the Inca Empire (Aufderheide 2003). In Egypt, the desiccation of the eviscerated body was achieved by the osmotic effect of powdered natron, composed of carbonate, bicarbonate and chloride salts of sodium (Aufderheide et al. 2004). Extensive resin

application to the body cavity lining as well as to the skin surface was performed to prevent soft tissue decay. Finally, the whole body was wrapped in linen bandages and placed in a coffin.

The mummification process leads to postmortem damage of ancient DNA (aDNA) through cleavage of base pairs and backbone damages. Studies at the Centre for Evolutionary Medicine, Institute of Anatomy at the University of Zurich, showed that the mean aDNA fragmentation is about 150 base pairs (bp's). Theoretically, the whole cell nucleus may possess 40 millions of such fragments if a cell consists of about 6×10^9 bp's. This direct effect of mummification is accompanied by significant reduction of oxygen and water content within cells, for instance, in cytoplasm. In mammalian cells, about 70 % of DNA damage is originated by indirect action of radiation from hydroxyl radicals for low-LET (linear energy transfer) radiation (Gunderson and Tepper 2012). In the present study, only dry ancient remains were considered, excluding any chemical and biochemical reactions.

Present paleopathology allows to gain knowledge on human health and medicine in ancient cultures. However, reconstructing the history of diseases (Aufderheide 2009) requires nondestructive methods for accurate analysis. Some researchers have used nonionizing imaging methods such as magnetic resonance or terahertz imaging to avoid damage to valuable genetic materials (Rühli et al. 2007; Öhrström et al. 2010). However, mostly ionizing imaging technologies such as X-ray, computed tomography (CT) and micro-CT are still employed today to investigate bioarcheological materials. In praxis, ionizing radiation has been extensively applied since the discovery of X-rays by W.C. Roentgen in 1895. X-ray radiography of human and animal mummies has a long tradition and was first performed by Koenig in 1896 (Koenig 1896).

In the early 1970s, development of CT revolutionized paleoradiology allowing three-dimensional (3D) imaging and surface-rendering capabilities. Such techniques have led to improvements in the diagnosis of paleopathological lesions and ancient skeletal remains (Chhem 2008). At present, CT has become the gold standard in radiological diagnosis because of its excellent contrast resolution of hard tissue and its availability in many hospitals. Consequently, anthropologists and forensic scientists have increasingly used clinical CT imaging with subsequent molecular diagnostics. Grieshaber and coworkers mention that in anthropology, "radiographic procedures are seen as nondestructive because there is no apparent damage to the specimen" (Grieshaber et al. 2008). Gray, for instance, stressed in a review of radiography that "radiography has no deleterious effect on a wrapped mummy" (Gray 1967).

In the past, many attempts were made to quantitate the impact of ionizing radiation on living cell cultures or on bacteria. For example, Grieshaber et al. studied the impact of CT imaging on bones from nine Sus scrofa (also called wild hog) feed and pointed out that, in their analysis, no statistical evidence existed that demonstrated that radiation decreased the amount of amplifiable DNA (Grieshaber et al. 2008). In many studies, radiation action on dry and wet cells was often investigated without considering the surrounding tissue (Incerti et al. 2009). The early assumption of target theory that the radiation sensitivity of target molecules is unaffected by surrounding molecules is, however, not correct (Braams et al. 1958). For this reason, it is important to demonstrate that the radiation sensitivity of desiccated cells is indeed affected by the surrounding medium, for example, different tissue types (Wilson 1959). Previous works demonstrated the degradation of dry and wet DNA following high doses of gamma rays, for example, kGy; the results were then extrapolated to low doses (Champlot et al. 2010). However, the change in radiation sensitivity of dry cells in tissue following mummification was never investigated.

It is well known from living cells that ionizing radiation may induce DNA damage by direct and indirect ionization of molecules. Photons, electrons and ions may ionize cell components along their tracks via the deposition of energy (Baccarelli et al. 2010). In addition, radicals produced in the presence of water may destroy cells by indirect action of ionizing radiation in normal tissue. Ionizations and excitations of atoms are caused by the photoelectric process and Compton scattering in the energy range typical for X-ray imaging. Such energy levels are high enough to affect the chemical binding of macromolecules, for example, aDNA. Direct action is a process where ionization and excitation of atoms take place directly in a cellular target (e.g., aDNA). In contrast, indirect action means that the DNA is affected by molecules of H_2O ionized and excited, for example, in cytoplasm. In addition, the produced radicals are very unstable; this leads to rearrangement of electronic configurations and to interactions with other molecules (Alpen 1998). Indirect ionization is observed mainly in living systems. We know that radiation may induce double-strand breaks (DSBs), which arise by increasing the level of unbound water in tissue. Similarly, oxygen and the presence of metabolic processes of cells increase radiosensitivity. Hutchinson pointed out that during the irradiation of macromolecules in a completely dry state, diffusible radicals are not formed (Hutchinson 1963). This fact precludes indirect action processes in desiccated cells. In general, desiccation of cells leads to a shrinkage of cell organelles due to osmotic stress, and, therefore, a decrease in cell volume (Kanias and Acker 2006). In addition, physical density increases because of an increase in intracellular salt concentration as a result of the desiccation process (Kanias and Acker 2006).

The role of environmental radiation

Besides man-made radiation exposure such as X-ray imaging, ionizing radiation from natural sources may also destroy ancient cells. Natural sources such as cosmic rays originating from space include energetic protons, electrons, gamma rays and X-rays (Environmental Protection Agency 2007). In terms of effective dose to humans, the major source of radiation exposure is radon gas and radon progeny, which comes from the decay of naturally occurring radium and emanates from the ground (Environmental Protection Agency 2007).

As an example of ground radiation, researchers have measured the maximum annual effective dose (MAD) in the Egyptian Serapeum Tomb in Saqqara. The total annual effective dose $\mathrm{MADtotal} = \mathrm{MAD(Radon)} + \mathrm{MAD(Thoron)} + \mathrm{MAD}(\gamma)$ for individuals working in this tomb was $12.7 \times 3 = 38.1$ mSv related to 24 h (Bigu et al. 2000). Note that this tomb showed the highest effective dose in comparison with other Egyptians tombs, for example, Ankh-Mahor tomb or Meriroka tomb (Bigu et al. 2000).

Recent measurements in Egyptian tombs indicate that the occupational radon exposure may even exceed the effective dose measured by Bigu. Gruber et al. showed that in tombs of the Valley of the Kings in Luxor, Egypt, occupational radon exposure ranges from 0.14 to about 77 mSv (90 days, 10-h working days) (Gruber et al. 2011). Because mummies do not inhale radon, however, only radon diffusion into ancient remains may be of relevance; this can be estimated by considering the one-dimensional transport equation, which describes radon diffusion in different materials (Chauhan et al. 2008). In ancient Egypt, bitumen and resin were used as ingredients for embalming of the body. By considering a diffusion length of radon in bitumen of $L = 0.7 \times 10^{-3}$ m (Keller and Hoffmann 2000) and the radon concentration of $N_0 = 12{,}000$ Bq/m^3 measured by Gruber et al. in tomb KV34 (Gruber et al. 2011), it can be shown that radon concentration in bitumen decreases rapidly to 165 Bq/m^3 at a depth of $x = 3$ mm (thickness of bitumen). Note that the one-dimensional transport equation describes the relationship between the radon concentration N at a distance x from the source, and N_0 is the concentration of the radon source, with $N = N_0 \exp(-x/L)$ (Chauhan et al. 2008). As a result of this estimate, because of the lack of inhalation and ingestion of mummies and because of the significant decrease in radon concentration in the embalming material, the effective dose to radon can be neglected.

The worldwide average annual effective dose from cosmic rays and terrestrial gamma rays is about 0.9 mSv (UNSCEAR 2010), which leads to an integrated effective dose of about 24 Sv to a mummy during a period of 27,000 years. In contrast, the effective dose due to an abdominal CT scan of living subjects lies in the range between 16 and 20 mSv (Unnik et al. 1997).

Independent of the radiation source and dose, geneticists have successfully studied nuclear and mitochondrial DNA from jawbone of a 27,000-year-old Sibirian mammoth (Poinar et al. 2006). Kefi found that "under favourable conditions, DNA can survive in tissue remains for several millennia and in some cases over 100,000 years" (Kefi 2011).

Keeping the expected natural radiation dose in mind, this sounds somewhat paradoxical and it gives rise to the question of what mechanisms might be responsible for the obvious low radiosensitivity of ancient cells and DNA fragments.

Therefore, the present study was conducted to understand the impact of ionizing radiation to ancient cells and DNA fragments. Because of the fact that CT imaging has reached the gold standard for 3D analysis of ancient remains, CT scans were simulated by Monte Carlo models.

In addition, actual doses in ancient remains due to X-ray imaging are unknown because the radiation protection principle **A**s **L**ow **A**s **R**easonably **A**chievable (ALARA 2013) is mostly not practised in paleoradiology. This means that ancient remains may receive a considerable higher X-ray dose than living subjects following CT imaging. Therefore, the intent of this work was to reduce the uncertainties in aDNA damage using X-ray imaging.

It is important to know that aDNA damage based on environmental radiation was never observed because of the difficulties in distinguishing between postmortem damage and DNA lesions invoked by environmental radiation.

Target theory

For the analysis of radiobiological effects on cells, the principle of hitting was formulated by the British physicist J. Crowther in 1924 (Crowther 1924). He noted that a target in radiobiology is a sensitive cellular structure that might be affected by one or several hits (ionizations).

The one-hit mechanism is based on the fact that a single ionization is sufficient to inactivate living organisms. Lea extended this principle to the target theory, which means that an irradiated object will be inactivated only when the hit fits the target of the volume v (Lea 1955). The quotient v/V is the hit probability, "where V is the total cellular volume" (Ballarini 2010). This theory assumes that physiochemical phenomena, which may be responsible for the radiation damage, will be produced directly in the target or in close vicinity, such as radical production, and electronic shell excitation (deMesquita et al. 2007). Because of the fact that "diffusible radicals are not formed in a completely dry state" (Hutchinson 1963), indirect radiation effects by biochemical reactions were not considered in the present work.

In general, the simple target theory was used in the past for the investigation of living cells under the constraints that no repair processes take place and radiation hits are random, which makes this theory applicable for the first time to study radiation tracks in ancient tissues and cells.

In the present study, hits are considered as events caused by particles passing through a sensitive site, for example, cells (Meyer et al. 1997). The Poisson law describes the statistic behavior of such events:

$$P(x) = (e^{-m}/x!)m^x \quad (1)$$

where $P(x)$ is the probability of the event x, and m represents the average hits per target. Equation 1 is extensively used in the present work to calculate the probability of hits on cell nuclei.

Microdosimetry

Simulation of radiation damage of cell nuclei presupposes a deep knowledge of microdosimetry. Reducing the size of a biological structure, for example, from cell to cell nucleus, leads to microscopic fluctuations of energy deposition in the target. The loss of proportionality of the classical quantity of absorbed dose at a microscopic level is considered here in the terms micro- and nanodosimetry.

In the present work, the specific energy in Gray is defined according to Rossi with $Z = \varepsilon/m_{\text{cell}}$ (J/kg), "where ε is the energy imparted by ionizing radiation to matter of mass m" (Rossi 1996). The mean energy E (eV) absorbed within the cell nucleus is calculated by a Monte Carlo algorithm using the conversion 1 eV = 1.602 10^{-19} J. The mass of the cell nucleus m_{cell} was calculated by multiplying the cell volume of an ellipsoid $v_{\text{cell}} = 4/3\pi abc$ (with abc, the semi-axes length) with the physical density ρ_{cell} of the cell phantom, that is, $m_{\text{cell}} = v_{\text{cell}}\ \rho_{\text{cell}}$.

Microscopic fluctuations of energy deposition increase as the dose decreases, the reference volume becomes smaller, and the ionizing radiation becomes denser. Gamma radiation is considered as sparsely ionizing, where the classical quantity of absorbed dose is acceptable in a wider range of dosimetry. Kellerer investigated the behavior of energy concentration of different radiation sources in small volumes and introduced the 20 % rule (Kellerer 1980). This rule indicates when the specific energy exceeds on average the absorbed dose by more than 20 %. The transfer from classical dosimetry to microdosimetry was considered in the present work by calculating the specific energy Z instead of the absorbed dose.

For the energy absorption in the nucleus, all interaction processes relevant in the energy range between 20 and 120 keV were considered, such as the Compton interaction or photoelectric interaction processes. Consequently, all important particles were considered, such as, photoelectrons, Compton electrons and scattered photons.

Role of mitochondrial DNA in forensic science

Mitochondrial DNA (mtDNA) is located outside of chromosomes in the mitochondria of the cell, which have several copies of the single mtDNA molecule. These organelles, which are located within the cytoplasm, are the energy producers of the cells.

In forensic science, mtDNA is an established resource for the "paleogenetic reconstruction of human evolution" (Parson 2009) because of its high copy number and increased stability against degradation (Parson 2009). So, in cases where conventional nuclear markers fail, mtDNA is employed to trace human evolution (Parson 2009).

Each mitochondrion possesses approximately two to 10 copies of mtDNA, while a single cell has 100 to many thousands of mitochondria. On the contrary, nuclear DNA (nDNA) contains only two copies in each cell (Saber-Khiabani 2012).

These large numbers of mtDNA copies have advantages in comparison with nDNA for genetic analysis, as one single cell may deliver a full mtDNA profile. Moreover, hair, bone or tooth samples from degraded skeletal remains or extremely small samples are sufficient to obtain a full mtDNA profile (Semikhodskii 2007). In addition, the circular genome makes mtDNA more stable over time (Beecher-Monas 2007) than nDNA.

The usefulness of mtDNA was tested in the late 1980s in the FBI Lab for human identity testing (Isenberg 2002). Knapp noted that the "analysis of aDNA was mostly restricted to short DNA fragments, usually derived from the mitochondrial genome" (Knapp and Hofreiter 2010).

Role of the polymerase chain reaction and Monte Carlo simulation

To date, biomolecular methods have been widely used in anthropology and forensic science because of biological analysis methods such as the polymerase chain reaction (PCR) (Mullis and Faloona 1987). However, this approach is extremely sensitive to DNA sequences, containing miscoding lesions from postmortem modifications, such as oxidative and hydrolytic degradations. An additional fragmentation of DNA-pieces caused by diagnostic X-ray imaging may shorten DNA fragments, which in turn makes the subsequent PCR amplification more difficult or even impossible. This further emphasizes the importance of increasing our knowledge about the radiosensitivity of ancient cells in tissue.

It is important to note that primary and secondary particles such as photons and electrons form tracks in tissue,

which show a nondeterministic behavior. In praxis, stochastic algorithms such as Monte Carlo (MC) codes have thus been employed for track structure studies. Consequently, the present work is based on MC simulations for the prediction of cell damage by application of the target theory. The use of MC simulations is the most popular method for modeling radiological imaging systems (Zaidi 2007).

Experimental works to determine the DNA fragmentation changes in dry tissue and cells following CT imaging were not documented in the past. The challenge of this task is not only to provide evidence of additional double-strand breaks in aDNA but rather to identify CT-induced new radiation damage from about 40 million postmortem DNA lesions in one ancient cell. The expected extremely low probability of additional DNA lesion in dry matter following X-ray imaging makes experiments less promising than simulations. The main advantages of MC simulation are, beside the cost and time effectiveness, the fact that different cell sizes and spacing's as well as different phantom materials can easily be investigated.

The overarching goal of the present project was to assist paleoradiologists who have to make decisions about the use of ionizing radiation in human remains with subsequent genetic analysis. More specifically, the aim was to assess the direct actions of ionizing radiation and to compare the effects of hits on cells embedded in normal tissue (e.g., muscle tissue) with those on cells in dry tissue phantoms following CT imaging. In addition, the hitting probability of secondary radiation, or secondaries, in different tissue phantoms and cells should also be investigated. By using the Poisson distribution, the probabilities of radiation damage in dry cells were calculated (Kellerer 1980).

Materials and methods

Monte Carlo toolkit

Several MC algorithms allow simulation of the interaction of particles with matter. However, only a few algorithms run on a workstation platform. The computer used in this study included an Intel Core i7 Extreme 980X processor (6 cores), 3.47 GHz, 12 MB RAM and a NVIDIA Quadro 4000 graphics card. The MC simulation was run under the operating system SUSE Linux Ver. 11.4 and was based on the open-source "GEometry ANd Tracking" toolkit Geant4 (Version 9.4 p01). This toolkit was developed by a world-wide collaboration of about 100 scientists (Agostinelli et al. 2003) for detector simulations in high-energy physics (HEP). The physics processes used here originated from the low-energy sub-package available in Geant4, which allows implementation of different physics and geometry classes in C++. The toolkit is an object-orientated set of libraries (Ivanchenko et al. 2012) able to simulate physical interactions with matter.

Important physics interactions to mimic X-ray imaging processes are the photoelectric effect and Compton scattering. In the present work, a new set of physics processes involving photons, electrons and positrons was implemented, which is called the Penelope (PENetration and Energy LOss of Positrons and Electrons) variants from the Geant4 sub-package (Physics Reference Manual 2010). The physics processes that were used here were called G4PenelopePhotoElectric and G4PenelopeCompton. Both processes were also designed for gamma particles down to low energies (100 eV) and could simulate cellular dosimetry and tracks of secondaries. For visualization, analyzing and debugging of the geometrical and physics models, the HepRep Browser (High Energy Physics REPresentables, 8 April 2007, Version 3.15.0) java tool was used (HepRApp 2012).

Validation of the Monte Carlo simulation

The MC simulations performed here were validated by calculation of absorbed doses in macroscopic phantom tissue due to real CT scans. Additionally, realistic X-ray source data, particle fluences and energy spectra (Xun et al. 2012) are essential for the accuracy of dose calculations and the determination of the number of hits in cells.

Computed tomography dose index

For validation of the MC simulations, the computed tomography dose index (CTDI) was employed. This index is an international standard for dose assessment (IEC 2002) in CT procedures and, therefore, often used for the validation of MC simulations (Kim et al. 2011). The CTDI is defined as the energy dose in a selected slice T (Eq. 2) and characterized by the typical dose profile originating from scattering processes along the z-axis.

$$\mathrm{CTDI}_{100} = \frac{1}{T}\int_{-50}^{50} D(z)\mathrm{d}z \tag{2}$$

where T is the slice thickness of 10 mm, D is the absorbed dose, and z is the axis of rotation (Kim et al. 2011). The range of the measured and simulated absorbed dose D was ± 50 mm.

For the determination of CTDI in real applications, the scattered radiation dose along the z-axis of a phantom cylinder placed in the isocenter of the CT scanner is measured.

Validation process

Two X-ray spectra, at 80 and 120 kVp/300 mAs, with an internal filtration of 2 mm Al, were generated by employing the online tool "xraygen." The mean energy of these spectra was 41.1 and 52 keV, respectively.

This tool is based on the Tungsten Anode Spectral Model using Interpolating Polynomials (TASMIP) model as described by Boone (Boone and Seibert 1997). We developed a geometric model to simulate the absorbed radiation dose at the isocenter of a cylindrical head phantom 16 cm in length and diameter. The phantom was composed of PMMA (polymethylmethacrylate $(C_5H_8O_2)_n$, with density ($\rho = 1.19$ g/cm3). We compared the measured absorbed dose $CTDI_m$ from a pencil ionization chamber with the simulated absorbed dose $CTDI_s$, in air and in PMMA (Tables 1, 2).

The integral in Eq. 2 describes the summation of all dose contributions collected ±50 mm away from the irradiated slice T. Consequently, a dosimeter was modeled consisting of 100 sensitive detectors ($dz = 1$ mm), placed in the center of the head phantom to calculate the simulated absorbed dose D along the z-axis.

To determine the normalization factor (NF), dose measurements and simulations were initially performed in air and the results were normalized to 300 mAs. According to Jarry, the NF is defined as

$$(\mathrm{NF})_{E,T} = \left(D_{\mathrm{Air,measured}}\right)_{E,T} / \left(D_{\mathrm{Air,simulated}}\right)_{E,T} \quad (3)$$

where NF is a function of beam energy E and slice thickness T, in units of photons/mAs (Jarry et al. 2003)

Table 1 summarizes the measured and simulated $CTDI_{100}$ values for various energies and the current time product of 300 mAs (Jarry et al. 2003). In the simulation, the phantom material of the cylinder was assigned as air where the absorbed dose in the sensitive detectors was calculated. Note that the normalization factors were used to convert simulated dose values (mGy/particle) to absolute dose values (mGy/mAs) (Jarry et al. 2003).

The dose differences between the simulated and measured results were determined for the PMMA phantom. The absolute dose was calculated using Eq. 4 (Jarry et al. 2003):

$$\left(D_{\mathrm{absolut}}\right)_{E,T} = (\mathrm{NF})_{E,T} \times \left(D_{\mathrm{simulated}}\right)_{E,T} \times (\mathrm{Total\ mAs}) \quad (4)$$

The relative difference Δ_{rel} was computed according to Eq. (5) using the simulated $CTDI_{100sPMMA}$ and measured CT dose index $CTDI_{100mPMMA}$

$$\Delta_{\mathrm{rel}} = \frac{\mathrm{CTDI}_{100\mathrm{sPMMA}} - \mathrm{CTDI}_{100\mathrm{mPMMA}}}{\mathrm{CTDI}_{100\mathrm{mPMMA}}} \times 100 \quad (5)$$

As shown in Table 2, the experimental results were in good agreement with those from the simulations.

Randomized distribution of cell nuclei in phantom tissues using three-dimensional self-avoiding random walk

For the investigation of polymer chains, the method of self-avoiding random walk (SAW) is often used (Freed 1981). This technique allows construction of cell clusters in a macroscopic environment. In this context, self-avoiding means no two cells occupy the same place within a coordinate system. A characteristic measure of a polymer chain is the mean-square end-to-end distance. In contrast to the classical random walk (RW), the mean-square displacement $\langle r^2 \rangle$ is not proportional to the time t, which is demonstrated in Fig. 1 (Berg 1993). Rather, the relationship can be written as $\langle (r_n - r_0)^2 \rangle = \langle r^2 \rangle \sim t^{\alpha}$ with $1 < \alpha < 2$ in Fig. 2. The probability to choose a walk in a 3D-RW cubic lattice model is 1/6. The developed GNU Octave (John W. Eaton and many others, version 3.4.3) program compares randomized 3D coordinates of each cell with the coordinates of previous walks to avoid different cells occupying the same coordinates. This effect is called "memory effect" of SAW and leads to the fact that the total number of possible walks is greatly reduced. For the MC simulation, the cell nucleus was embedded in chemically realistic phantom materials.

Table 1 Measured and simulated $CTDI_{100}$ in air at the isocenter, in a cylindrical phantom

Beam energy (kVp)	Measured $CTDI_{100m\_air}$ (mGy/300 mAs)	Simulated $CTDI_{100s\_air}$ (10^{-11} mGy/particle)	Normalization factor (NF) (10^9 photons/mAs)
80	24.00 ± 0.96*	5.82	1.37
120	61.14 ± 2.45*	8.99	2.27

The simulated X-ray source (fan-beam with 10^7 photons) was located at a distance of 100 cm SIC (source-to-isocenter), slice thickness 10 mm. $CTDI_{100m\_air}$: measured CT dose index at 100 mm length in air; $CTDI_{100s\_air}$: simulated CT dose index at 100 mm length in air

* (Jarry et al. 2003); for details, see text

Table 2 Measured and simulated $CTDI_{100}$ in PMMA at the isocenter

Beam energy (kVp)	Measured $CTDI_{100m\_PMMA}$ (mGy/300 mAs)	Simulated $CTDI_{100s\_PMMA}$ (mGy/300 mAs)	Relative difference Δ_{rel} (%)
80	9.3*	8.92	−4.08
120	31.0*	31.3	0.97

$CTDI_{100m\_PMMA}$: measured CT dose index at 100 mm length in PMMA *; $CTDI_{100s\_PMMA}$: simulated CT dose index at 100 mm length in PMMA; Δ_{rel}: relative difference between measured CTDI and simulated CTDI *: (Jarry et al. 2003); for details, see text

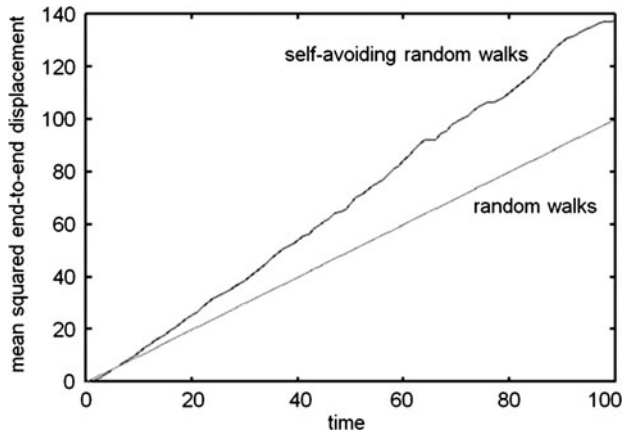

Fig. 1 Mean squared end-to-end distance grows with the power of α; $\alpha = 1$ for random walk (i.e., linear growth), and $\alpha = 1.07$ for self-avoiding walk

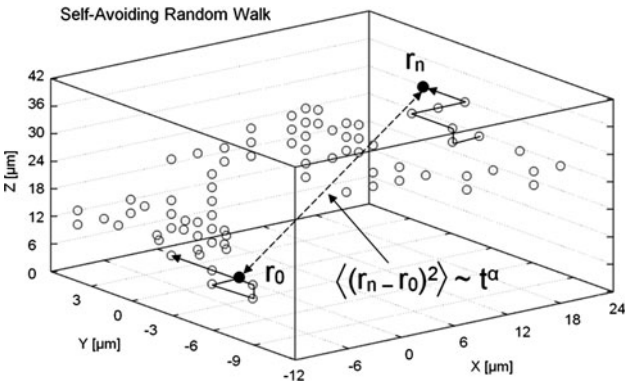

Fig. 2 Self-avoiding random walk algorithm mimics the distribution of 85 cells (*circles*), which are embedded in a cubic lattice (grating constant 3 μm) volume. The mean end-to-end distance $<(r_0 - r_n)^2>$ is about 35 μm

Cell models and phantom materials

To make our cell models more realistic, we considered different cell densities typical for muscle tissue and bone tissue. The dehydration process was considered using smaller cell sizes, for instance, ellipsoids with the diameter of 4 μm and the length of 6 μm (Fig. 3).

A cluster of 85 randomly distributed cell nuclei (Fig. 2) were positioned in a cylinder (Fig. 4) with a diameter and length of 10 mm at the isocenter of a CT scanner model.

The cell nuclei consisted of protein, where the chemical formula was assumed to be $C_{100}H_{159}N_{26}O_{32}S$, and the density $\rho = 1.34$ g/cm^3 (Wang et al. 2003). Nuclei were defined as a sensitive volume where the specific energy and the average number of hits were calculated.

The dehydration process of cells was initially investigated in-house by histological methods with samples of mummified remains. Cell size and cell density were defined based on these studies, which led to the development of two different cell sizes and spacing.

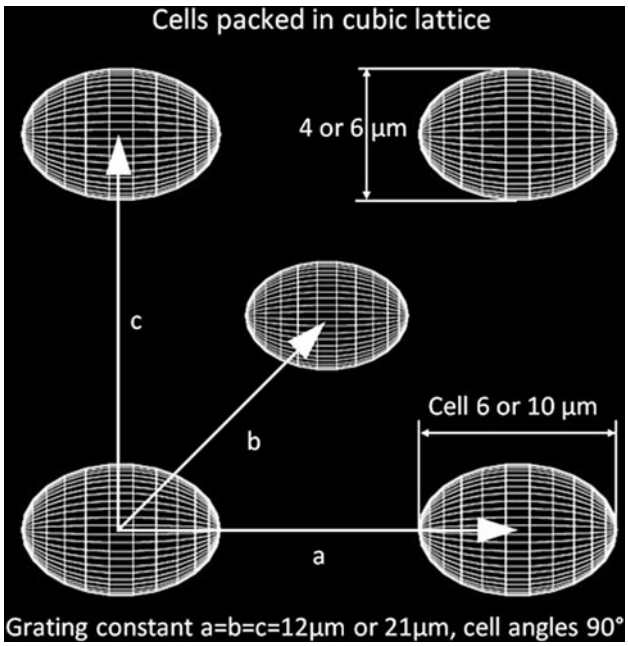

Fig. 3 Model of five cell nuclei represented by ellipsoids and packed in a cubic lattice. The mummification process was considered by two different cell sizes and two different cell densities

Figure 3 depicts two cell sizes, $4 \times 4 \times 6$ μm^3 and $6 \times 6 \times 10$ μm^3, with the variation of the grating constant to realize two different cell densities of about 1×10^8 cells/cm^3 for cortical bone (CB) cells and a higher density of about 5.7×10^8 cells/cm^3 for muscle cells.

The cylinder in Fig. 4 consisted of anthropomorphic materials such as CB taken from the Geant4 Material Database (Geant4 Material Database 2012) [G4_BONE_CORTICAL_ICRP (1.85 g/cm^3)] normal muscle tissue (NT) composed of $C_5H_{40}O_{18}N$ ($\rho = 1.06$ g/cm^3) (Constantinou et al. 1982) and dry muscle tissue (DT) composed of C_5H_6ON ($\rho = 1.35$ g/cm^3) which was deduced from NT by removing 17 H_2O molecules from $C_5H_{40}O_{18}N$, because ancient tissue is not fully dehydrated. Because we were mainly interested in the volume reduction and density change following dehydration, we calculated the molecular weight (MW) of 17 water molecules ($MW_{H2O} = 18.02$ g/mol $\times$ 17 = 306.34 g/mol) to get the volume per mol $V_{17\ H2O} = MW_{H2O}/\rho_{H2O} = (306.34\ \text{g/mol})/(1\ \text{g/cm}^3) = 306.34$ cm^3/mol. Next, the volume per mol for the normal tissue phantom $V_{C5H40O18N} = MW_{C5H40O18N}/\rho = 402$ g/mol/1.06 g/cm^3 = 379 cm^3/mol was calculated. Accordingly, the volume reduction due to dehydration was $V_{C5H6ON} = V_{C5H40O18N} - V_{17\ H2O} = 379$ cm^3/mol – 306.34 cm^3/mol = 72.66 cm^3/mol.

Finally, the increase in physical density of muscle tissue following dehydration was calculated using the molecular weight of MW_{C5H6ON} (96.1 g/mol) from an online molecular calculator (FU 2013). Hence, the increase in

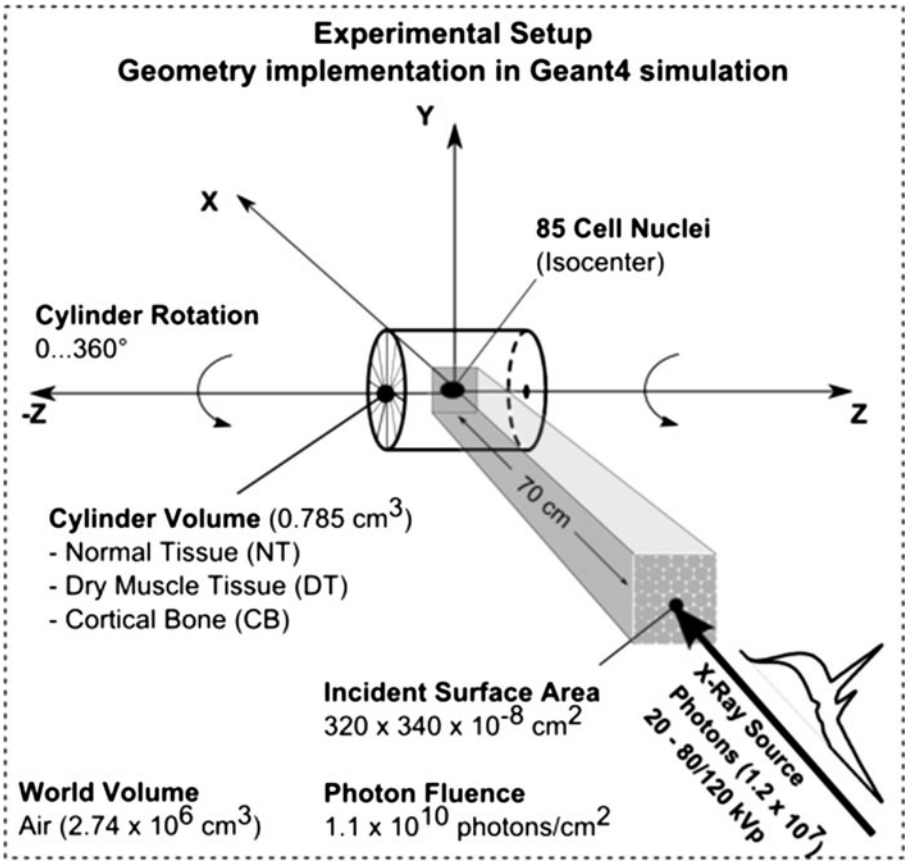

Fig. 4 Experimental setup from a GEANT4 simulation showing, from front to back, the X-ray source spectrum from 20 to 80 kVp and 120 kVp with the photon fluence, the isocenter where cells are placed according to the self-avoiding walk (SAW) and the cylinder that contained anthropomorphic phantom tissues, for example, normal tissue (NT), dry muscle tissue (DT) or cortical bone (CB)

physical density following dehydration was $\rho_{C5H6ON} = MW_{C5H6ON}/V_{C5H40O18N} = (96.1\ g/mol)/(72.66\ cm^3/mol) = 1.32\ g/cm^3$. This result is in good agreement with published data, where the density of dry tissue was taken to be $1.35\ g/cm^3$ (Gu 2003).

Compound molecules could be defined as being composed of one or more elements in the desired proportion. For instance, the world volume that contained air was created as a mixture of N (70 %) and O (30 %) with $\rho = 1.290\ mg/cm^3$.

The irradiated cylinder depicted in Fig. 4 was rotated from 0 to 360° with a step size of 10° to get an isotropic exposure of randomly distributed cell nuclei.

The X-ray source was modeled as a parallel beam and positioned in the x-direction at a distance of 70 cm from the isocenter. The cylinder and X-ray source were located within the world volume (air volume around the sample cylinder). The spectrum of the X-ray source originated from the validation process. Within the cell nuclei representing the targets, the specific energy and hit rate were calculated.

Statistical analysis

Data were separately analyzed for two different X-ray energies and different phantom tissues such as NT, DT, CB and two cell nuclei sizes. The cell hit probability of zero, one or more (n) hits, that is, $P(0)$, $P(1)\ldots P(n)$, was calculated by Eq. 1, where m represented the mean of all affected nuclei at 0–360° in the tissue phantom.

All 85 targets were placed in the isocenter of a CT scanner model. Each energy deposition within the cell nucleus was counted and the number of these nuclei was called "number of affected targets." Poisson distribution and the boxplot were processed by the statistical package, R version 2.15.1 (GNU project).

Finally, all secondary electrons were counted in the area of the cell cluster to quantitate the type of interaction process (e.g., photoabsorption, Compton scattering) in all tissue phantoms.

Results

Table 3 summarizes the results obtained for the different phantom tissues, cell sizes and photon energies. Because cell nuclei are characterized by microvolumes, the specific energy Z in Table 3 represents a stochastic quantity which can differ considerably from a nonstochastic quantity such as the dose D (Kudryashov 2008). In addition, Table 3 also summarizes the results of the Poisson distribution for unaffected nuclei $P(0)$.

Table 3 Probability of unaffected nuclei $P(0)$ and the specific energy Z as a function of the incident photon energy, cell size and density (6610: $6 \times 6 \times 10$ μm^3 with 21 μm cell spacing; 446: $4 \times 4 \times 6$ μm^3 with 12 μm cell spacing)

Tissue types	$P(0)$	ε (keV) μ ± SD	Z (Gy) μ ± SD
Photon energy at 80 kVp			
NT6610	0.41	624 ± 91	0.397 ± 0.06
DT6610	0.43	515 ± 94	0.327 ± 0.06
CB6610	0.85	58 ± 26	0.037 ± 0.02
NT446	0.59	173 ± 44	0.412 ± 0.1
DT446	0.64	134 ± 45	0.319 ± 0.1
CB446	0.93	20 ± 14	0.048 ± 0.03
Photon energy at 120 kVp			
NT6610	0.51	260 ± 64	0.17 ± 0.04
DT6610	0.53	239 ± 63	0.15 ± 0.04
CB6610	0.43	365 ± 74	0.23 ± 0.05
NT446	0.72	71 ± 28	0.17 ± 0.07
DT446	0.74	66 ± 26	0.16 ± 0.06
CB446	0.52	266 ± 66	0.63 ± 0.16

NT normal tissue, *DT* dry tissue, *CB* cortical bone, *SD* standard deviation, ε the mean absorbed energy in cell

Monte Carlo simulation with 80 kVp photons

The impact of tissue shrinkage, that is, DT6610 to DT446, as well as the change of material properties, is shown in Fig. 5. The boxplot illustrates the number of affected targets embedded in different phantom materials at 80 kVp. Figure 5 is useful for comparing the number of affected targets for different tissue types and cell sizes.

The histograms in Fig. 6 depict results of the simulation with low-energy photons penetrating the sample cylinder composed of NT and DT. Note the different sizes of the cell phantoms that may demonstrate the mummification process. Note that only the direct action of radiation on the phantom material of interest was considered.

Figure 7 illustrates secondary particles produced by photon interactions with tissue atoms in the sample cylinder. The generated tracks of electrons originate mainly from photoelectrons (Fig. 8), with a path length from 2 to 10 μm, which corresponds roughly to a kinetic energy from 15 to 19 keV in DT or CB. Note the different path lengths of secondary tracks in air (outside the sample cylinder) and around the cell cluster in the center of the samples.

The distribution of the physical dominant processes in phantom tissues at 80 kVp is reflected in Fig. 8.

Monte Carlo simulation with 120 kVp photons

With increasing X-ray energy, Compton scattering becomes more dominant. Similar to the case of the 80 kVp X-ray source (Fig. 5), Fig. 9 shows the corresponding results for the 120 kVp X-ray source.

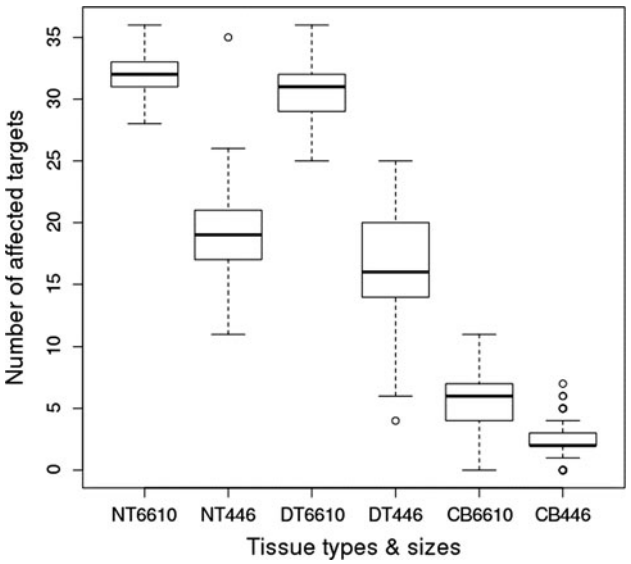

Fig. 5 Median of affected nuclei at 80 kVp for three different tissue phantoms [normal tissue (NT), dry tissue (DT) and cortical bone (CB)] and two different sizes [$6 \times 6 \times 10$ μm^3 (6610) and $4 \times 4 \times 6$ μm^3 (446)]. The *boxplot* depicts the number of hits per tissue type and size at 80 kVp. The upper and lower margins of the *box* represent the 75th and 25th percentiles, respectively. The median is represented by the *middle line*. Minimal and maximal values above and below the *boxes* are indicated by *vertical lines* with *whiskers*. *Open circles* depict outliers. *Bold circles* indicate additional outliers at the same position

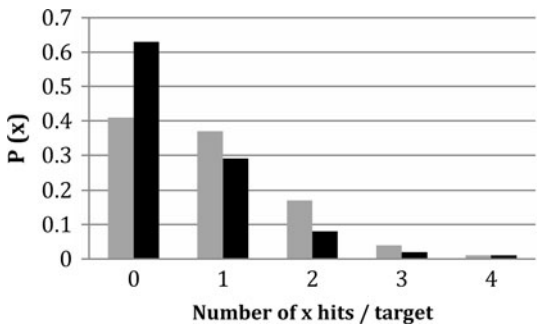

Fig. 6 Probability $P(x)$ of hit cell nuclei with different sizes embedded in normal (NT, *gray*) and dry (DT, *black*) phantom tissue using 80 kVp X-rays and two different cell sizes [$6 \times 6 \times 10$ μm^3 (6610) and $4 \times 4 \times 6$ μm^3 (446)]

In order to compare with Fig. 6, Fig. 10 summarizes the difference between the affected $P(1..4)$ and nonaffected targets $P(0)$ of DT and NT from the 120 kVp X-ray source, that is, using photon energies similar to those used for clinical imaging. Again, the mummification process was considered by reducing cell size and spacing, and the direct action of radiation was considered.

Figure 11 highlights the results obtained in DT and CB, that is, secondary electrons leaving the sample volume by forming stochastic tracks in air (see Fig. 7 for comparison).

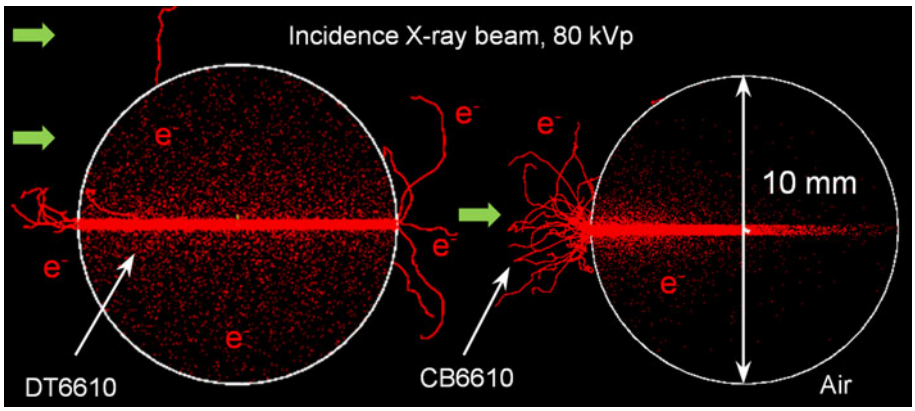

Fig. 7 Tracks of secondary electrons (*red*) in dry tissue (DT, *left*) and cortical bone (CB, *right*). Because of the small size of the targets, the cell cluster in the center of the *circles* is invisible. Note the increased backscattered electrons in high Z CB material on the right and the exponential decrease in energy absorption with depth. The 80 kVp X-ray source was positioned on the *left side* (*green arrows*) of the *circles*. The number of source photons was limited to 120×10^3 to reduce the load of the workstation

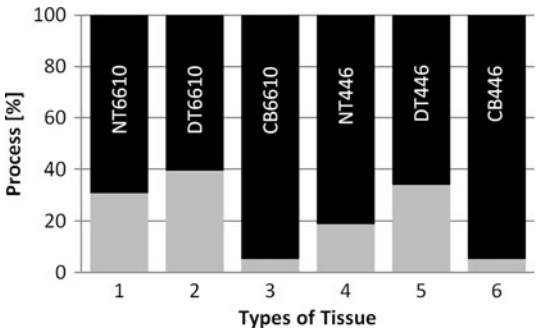

Fig. 8 Photoabsorption (*black*) versus Compton scattering (*gray*) of three different phantom tissues [normal tissue (NT), dry tissue (DT), and cortical bone (CB)] and two different cell sizes [$6 \times 6 \times 10$ μm^3 (6610) and $4 \times 4 \times 6$ μm^3 (446)] for 80 kVp photons

Similar to Fig. 8 for 80 kVp photons, the distribution of the physics processes for 120 kVp photons is depicted in Fig. 12. All defined tissue phantoms, sizes and cell densities were considered.

Discussion

Based on a literature review, we hypothesized that mummified cells in dry tissue might be less radiosensitive than cells in normal tissue, because of their reduced size and spacing. The term "less radiosensitive" does not necessarily mean lower deposited dose, because the distribution of the absorbed energy around the cell nuclei following low-dose exposure is also important. Note that the present work was focused on the simple target theory of radiobiology, which implies that no DNA damage occurs in unexposed cell nuclei. Moreover, cell spacing also plays an important role in the context of the path length of secondary particles, such as photoelectrons or recoil electrons, due to Compton scattering. For instance, if a photon hits a nucleus embedded in CB6610 at 80 kVp and a photoelectric absorption takes place, then the photoelectron is not able to hit an adjacent nucleus because its path length, as was demonstrated in the present study, is smaller than 10 μm. Thus, the term "radiosensitivity" refers here to the number of cell hits within a certain tissue rather than to the absorbed dose, because the absorbed dose is a macroscopic quantity and the energy transfer from one cell hit to the other was different by the order of three. Note that the absorbed energy was dominant between cell nuclei, and their contribution to the radiosensitivity of cell nuclei is, therefore, small. In addition, the small variability of cell hits makes this quantity more suitable as a metric for the radiosensitivity of cells in comparison with the absorbed dose.

Simulated cell irradiation using 80 kVp X-rays

Reducing cell size and spacing from NT to DT lead to an increased probability of unaffected targets $P(0)$ from 0.41 to 0.64 (Fig. 6). This increase originates from the fact that the nuclei were smaller for DT446 than for NT6610, and less so from the higher atomic number of DT compared to NT (about 30 %). In general, the number of hits decreased significantly in cells embedded in high-density material, such as cortical bone (Fig. 5). The decreased number of hits is associated with a lower energy of incident photons as well as with a decrease in kinetic energy of secondary electrons, resulting in a shorter mean track length of electrons of about 2.6 μm in CB compared to 5 μm in DT. Moreover, a considerable proportion of secondary electrons in CB were backscattered in surface layer of the cylinder because of the low photon incident energy (Fig. 7). These results are consistent with those of Kudryashov who showed that soft Roentgen rays with energies less than 100 keV are absorbed in surface layers of tissue due to photoelectric interaction (Kudryashov 2008).

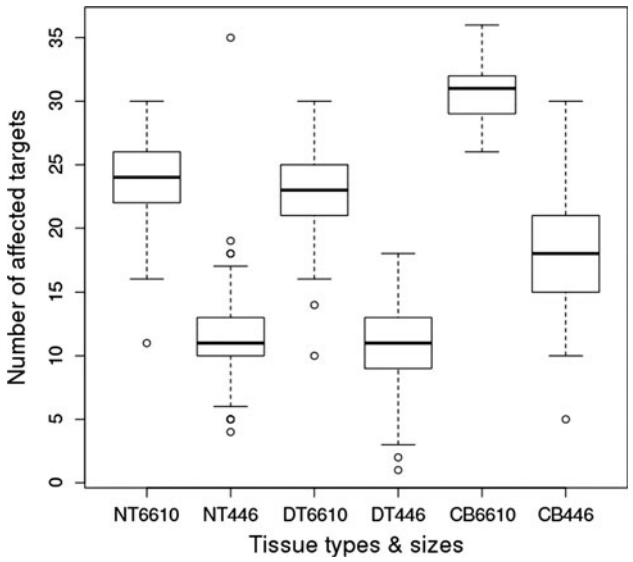

Fig. 9 Median of affected nuclei at 120 kVp for three different tissue phantoms [normal tissue (NT), dry tissue (DT) and cortical bone (CB)] and two different sizes [$6 \times 6 \times 10$ μm^3 (6610) and $4 \times 4 \times 6$ μm^3 (446)]. The boxplot depicts the number of hits per tissue type and size at 120 kVp. The upper and lower margins of the *box* represent the 75th and 25th percentiles, respectively. The median is represented by the *middle line*. Minimal and maximal values above and below the *boxes* are indicated by *vertical lines* with *whiskers*. *Open circles* depict outliers. *Bold circles* indicate additional outliers at the same position

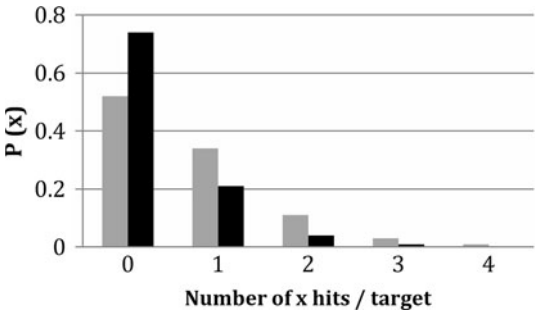

Fig. 10 Probability $P(x)$ of hit cell nuclei with different sizes embedded in normal (NT, *gray*) and dry (DT, *black*) phantom tissue using 120 kVp X-rays and two different cell sizes [$6 \times 6 \times 10$ μm^3 (6610) and $4 \times 4 \times 6$ μm^3 (446)]

In addition, photoabsorption results in a higher energy deposition in all phantoms compared with Compton scattering, because the incident photon energy is absorbed in atoms. Accordingly, at 80 kVp, photoabsorption is the dominant physics process with the mean of 77.7 ± 14 % and especially in CB tissue with higher atomic number Z (Fig. 8). Note that the dependence of photoabsorption on energy and atomic number is often expressed as the probability $P \approx Z_{\text{eff}}^4/E^3$, where Z_{eff} represents the effective atomic number of the compound material and E the kinetic energy of the photons.

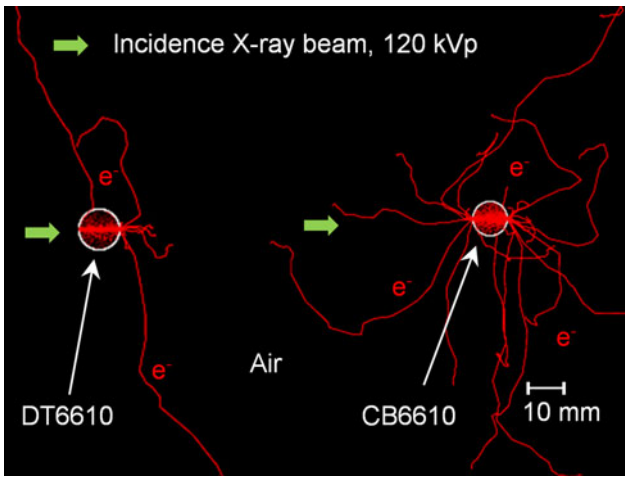

Fig. 11 Tracks of secondary electrons (red) in dry tissue (DT, left) and cortical bone (CB, right). The 120 kVp X-ray source was positioned on the left side (green arrows). The number of source photons was limited to 120×10^3 to reduce the load of the workstation

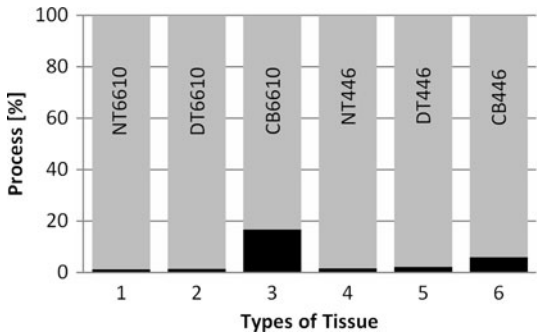

Fig. 12 Compton scattering (*gray*) versus photoabsorption (*black*) of three different phantom tissues [normal tissue (NT), dry tissue (DT) and cortical bone (CB)] and two different cell sizes [$6 \times 6 \times 10$ μm^3 (6610) and $4 \times 4 \times 6$ μm^3 (446)], for 120 kVp photons

The present simulations showed that, in agreement with Goodhead, the energy depositions in all cells were caused by single independent tracks and not by multitracks (Goodhead and Nikjoo 1989). Figure 13 demonstrates the dominant physics process in this energy range by a single photon and electron track. Note that the simulated kinetic energy of the photoelectron was assessed through the calculation of the effective atomic number Z_{eff} of the protein and the binding energy of the K-shell (E_{K}). For instance, the initial kinetic energy IKE of the secondary electron was calculated by subtracting E_{K} from the incident photon energy. The binding energy of the K-shell was calculated by $E_{\text{K}} = R \times Z_{\text{eff}}^2(1/n^2 - 1/m^2) = 0.48$ eV, where R is the Rydberg energy of 13.6 eV, and m, n represent energy states of the atom. For the example shown in Fig. 13 where the initial kinetic energy of the photon is 18.1 keV, the

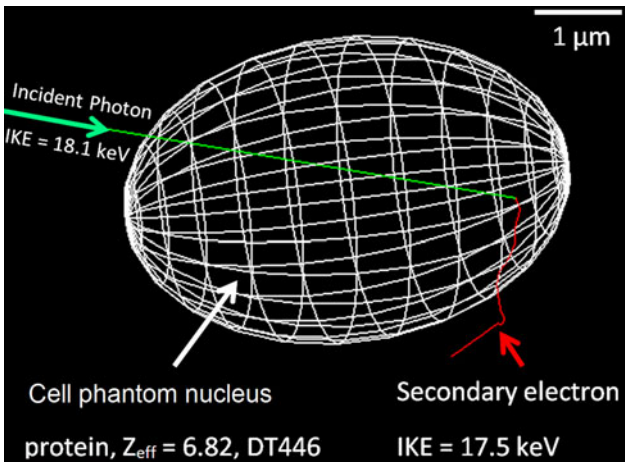

Fig. 13 Simulated photoabsorption with a photon from the 80 kVp X-ray source. The cell phantom was embedded in dry tissue (DT) and had a size of 4 × 4 × 6 µm^3 (446) to mimick a dehydrated nucleus. Note the short track length of about 4 µm of the secondary electron. *IKE*: initial kinetic energy

simulated kinetic energy of the secondary electron is 18.1 keV − 0.48 keV = 17.62 keV, which is a good approximation to our simulation energy of 17.5 keV.

The energy absorption due to Compton scattering was not significant because of the small kinetic energy of recoil electrons of about 1 keV and their short mean track length <<1 µm.

Simulated cell irradiation using 120 kVp X-rays

Due to the increase in photon energy (from 80 to 120 kVp), Compton scattering became the dominant process (95 ± 5 %) (Fig. 12) which led to a further increase in unaffected targets to 74 % at DT446 (Fig. 10). Interestingly, and similar to the 80 kVp case, the number of unaffected targets rose from NT6610 to DT446 by 23 %. Finally, the probability to hit a target once or twice was <30 % (Fig. 10) for DT.

In the domain of Compton scattering, we observed lower energy absorption for NT and DT, while noticing an increase in the specific energy in high Z material of CB (Table 3, photon energy at 120 kVp) in comparison with the photon energy at 80 kVp. This may be due to the reduced backscattering of photoelectrons and the higher kinetic energy of Compton recoil electrons at 120 kVp in comparison with photoelectrons at 80 kVp (Table 3; Fig. 7).

In general, the pairwise comparison of NT with DT showed a decrease in affected targets in both energy ranges, for DT (Figs. 6, 10). This effect is caused mainly by the reduced target volume of DT cells compared to NT cells and less by the increased density of DT.

Probabilities of ancient DNA damage

Paleopathologists are mainly interested in the damage of aDNA. It is known that only 2 % (P_{DNA}) of the cell nucleus includes DNA molecules. Accordingly, at 80 kVp, the probability of DNA damage is $P_{\mathrm{DNAdamage80}} = \{1 - P(0)\} \times P_{\mathrm{DNA}} = 0.36 \times 0.02 \approx 0.007$, while at 120 kVp, the probability of DNA damage is $P_{\mathrm{DNAdamage120}} = \{1 - P(0)\} \times P_{\mathrm{DNA}} = 0.26 \times 0.02 \approx 0.005$, for dry tissue (DT446).

To consider the volume effect, one can repeat these calculations using the size of normal cells (DT6610). The probability of DNA damage in normal cell volume is then $P_{\mathrm{DNAdamage80}} = \{1 - P(0)\} \times P_{\mathrm{DNA}} = 0.57 \times 0.02 \approx 0.011$ at 80 kVp, and $P_{\mathrm{DNAdamage120}} = \{1 - \mathrm{P}(0)\} \times P_{\mathrm{DNA}} = 0.47 \times 0.02 \approx 0.009$ at 120 kVp.

The most significant outcome is that the probabilities of DNA damage decrease for smaller cells with the differences $\Delta P_{\mathrm{DNAdamage80}} = (0.011_{6610} - 0.007_{446}) = 0.004$ (4 ‰) and $\Delta P_{\mathrm{DNAdamage120}} = (0.009_{6610} - 0.005_{446}) = 0.004$ (4 ‰) by decreasing the cell size from DT6610 to DT446.

Note that these results were based on nuclei composed of unfragmented DNA. Moreover, the investigation of the indirect action of ionizing radiation was beyond the scope of this work. However, according to Repine, 30 % of DNA breaks in normal cells results from direct action of radiation on the DNA for low-LET radiation (Roots and Okada 1972; Okada 1970). Consequently, the lower radiosensitivity of dry cells results from reduced volumes of remaining nuclei and from the high fragmentation of aDNA (e.g., approximately 40×10^6 DNA fragments within the ancient nucleus may occur).

Note that increasing DNA fragmentation in ancient remains is associated with decreasing probability of DNA DSB's. Equation 6 describes the relationship between cell hits ($j = \{0, 1, 2, \ldots, 4\}$) and the probability to hit k-DNA fragments. Note that DNA fragmentation divides the normal DNA in many small target volumes of approximately $V_{\mathrm{DNA}} < 80$ nm^3 at 150 bp, which are distributed around the center of the cell nucleus. According the Poisson distribution in Figs. 6 and 10, the number of cell hits was restricted to $j \leq 4$ in Eq. 6.

$$p_{(j\leq 4)} = \left[\{1 - \sum_{j=0}^{n} p(j)\} \times P_{\mathrm{DNA}}\right]^k \qquad (6)$$

(6)where k is the number of DNA fragments per cell $k = \{1, 2, 3, \ldots, m\}$ and $P_{\mathrm{DNA}} = V_{\mathrm{DNA\text{-}fragment}}/V_{\mathrm{cell\text{-}nucleus}}$.

As a result, the power function in Eq. 6 indicates that the higher the DNA fragmentation in ancient cells, the higher the number of unaffected DNA fragments following CT imaging.

Most importantly, in dry cells, indirect action of radiation can be considered as not relevant.

Conclusions

In this study, the effect of ionizing radiation on cells following mummification was investigated, to address the main question of this paper: How does the mummification process change the radiation sensitivity of cells following low-dose exposure?

Models were here described to simulate the impact of CT imaging on normal and shrunken cell structures in different phantom tissues. By studying the direct action of ionizing radiation, existing approaches were extended to dry cells by considering also the tissue between the cells under realistic CT conditions. Three tissue phantoms, NT, DT and CB, were compared and the impact of cell shrinking and spacing was studied.

The study clearly demonstrated a significant decrease in radiosensitivity of irradiated cells under mummified conditions. This result indicates that factors such as cell size and spacing as well as tissue density influence the number of affected cells. It is important to emphasize that the number of unaffected cells has increased by 23 % for both 80 and 120 kVp photons, by changing the tissue material from NT to DT. The maximum number of unaffected targets $P(0)$ was 74 % at 120 kVp for DT.

In the lower energy range, the photoelectric process predominated. There, photoabsorption in CB leads to an exponential decrease in absorbed energy with depth, which protects cells in deeper layers against radiation exposure. Consequently, the probability of unaffected cells rose rapidly to 93 % in cortical bone, at 80 kVp.

In addition, it was demonstrated that the probability of damage of unfragmented DNA in dry tissue (DT446) decreased further with $P \approx 0.007$ at 80 kVp and $P \approx 0.005$ at 120 kVp, respectively.

These results support the hypothesis that mummified and shrunken cells are more radioresistant than cells with normal volume. Note that here only the direct action of ionizing radiation was discussed (e.g., 30 % of radiation-based DNA breaks). In addition, it was considered that aDNA may be extremely predamaged by postmortem processes such as hydrolytic and oxidative damage, which leads to the conclusion that additional DNA strand breaks by radiation damage from CT imaging are insignificant.

Future studies will focus on the radiation damage of highly fragmented DNA in desiccated cell nuclei. More basic research is necessary to understand the mummification process in detail. This may lead to more realistic models of dry cells or DNA in future simulations.

Acknowledgments We gratefully acknowledge Béhnaz Jarrahi, from the Institute of Neuroradiology at the University Hospital Zurich in Switzerland, for manuscript proofreading and suggestions. We would like to acknowledge the Mäxi-Stiftung in Zurich for their generous support.

References

Agostinelli S, Allison J, Amako K, Apostolakis J, Araujo H, Arce P et al (2003) Geant4—a simulation toolkit. Nucl Instrum Methods A 506(3):250–303

ALARA (2013) As low as reasonable achievable. http://www.nrc.gov/reading-rm/basic-ref/glossary/alara.html. Accessed 8 Feb 2013

Alpen EL (1998) Radiation biophysics, 2nd edn. Academic Press, San Diego

Aufderheide AC (2003) The scientific study of mummies, 1st edn. Cambridge University Press, Cambridge

Aufderheide AC (2009) Reflections about bizarre mummification practices on mummies at Egypt's Dakhleh oasis: a review. Anthropol Anz 67(4):385

Aufderheide AC, Cartmell L, Zlonis M, Sheldrick P (2004) Mummification practices at Kellis Site in Egypt's Dakhleh Oasis. JSSEA 31

Baccarelli I, Gianturco FA, Scifoni E, Solov'yov AV, Surdutovich E (2010) Molecular level assessments of radiation biodamage. Eur Phys J D60:1–10

Ballarini F (2010) From DNA radiation damage to cell death: theoretical approaches. J Nucleic Acids 2010:350–608

Beecher-Monas E (2007) Evaluating scientific evidence: an interdisciplinary framework for intellectual due process. Cambridge University Press, Cambridge

Berg HC (1993) Random walks in biology. Princeton University Press, Princeton, p 152

Bigu J, Hussein MI, Hussein AZ (2000) Radiation measurements in Egyptian pyramids and tombs—occupational exposure of workers and public. J Environ Radioact 47:245–252

Boone JM, Seibert JA (1997) An accurate method for computer-generating tungsten anode x-ray spectra from 30 to 140 kV. Med Phys 24(11):1661–70

Braams R, Hutchinson F, Ray D (1958) Changes in the sensitivity of enzymes in the dry state to radiation. Nature 182(4648):1506

Champlot S, Berthelot C, Pruvost M, Bennett EA, Grange T, Geigl EM (2010) An efficient multistrategy DNA decontamination procedure of PCR reagents for hypersensitive PCR Applications. PLoS ONE 5(9):e13042. doi:10.1371

Chauhan RP, Nain M, Kant K (2008) Radon diffusion studies through some building materials: effect of grain size. Radiat Meas 43:S445–S448

Chhem RK (2008) PaleoRadiology imaging mummies and fossils. Springer, Heidelberg

Constantinou C, Attix FH, Paliwal BRA (1982) Solid water phantom material for radiotherapy X-ray and gamma-ray beam calibrations. Med Phys 9:436–441

Crowther JA (1924) Some considerations relative to the action of x-rays on tissue cells. Proc R Soc Lond (Biol) 96:207–211

deMesquita CH, Neto JMF, Hamada MM (2007) Target theory applied in the radiation damage analysis for organic detectors. Nuclear Science Symposium Conference Record 2:1313–1317

Environmental Protection Agency (2007) Ionizing Radiation Fact Book, EPA-402-F-06-061

Freed KF (1981) Polymers as self-avoiding walks. Ann Prob 9(4): 537–556

FU (2013) Freie Universität Berlin. http://www.chemie.fu-berlin.de/cgi-bin/molform. Accessed 4 Feb 2013

Geant4 Material Database (2012) chapter 8, Appendix http://geant4.web.cern.ch/geant4/UserDocumentation/UsersGuides/ForApplicationDeveloper/html/apas10.html. Accessed 22 July 2012

Goodhead DT, Nikjoo H (1989) Track structure analysis of ultrasoft X-rays compared to high- and low-LET radiations. Int J Radiat Biol 55:513–529

Gray PHK (1967) Radiography of ancient Egyptian mummies. Med Radiogr Photogr 43:34–44

Grieshaber BM, Osborne DL, Doubleday AF, Kaestle FA (2008) A Pilot study into the effects of X-ray and computed tomography exposure on the amplification of DNA from bone. J Archaeol Sci 35(3):681–687

Gruber E, Salama E, Rühm W (2011) Real-time measurement of individual occupational radon exposures in tombs of the Valley of the Kings, Egypt. Radiat Prot Dosim 144(1–4):620–626

Gu WY (2003) Effects of hydration and fixed charge density on fluid transport in charged hydrated soft tissues. Ann Biomed Eng 31:1162–1170

Gunderson LL, Tepper JE (2012) Clinical radiation oncology. Elsevier Saunders, Philadelphia

HepRApp (2012) HepRep browser Application. http://www.slac.stanford.edu/~perl/HepRApp. Accessed 5 Sept 2012

Hutchinson F (1963) Radiation effects on macromolecules of biological importance. Annu Rev Nu Sci 13:535–564

IEC (2002) Medical electrical equipment: part 2-44. Particular requirements for the safety of x-ray equipment for computed tomography. IEC 60601-2-44

Incerti S, Seznec H, Simon M, Barberet P, Habchi C, Moretto P (2009) Monte Carlo dosimetry for targeted irradiation of individual cells using a microbeam facility. Radiat Prot Dosim 133(1):2–11

Isenberg AR (2002) Forensic mitochondrial DNA analysis: a different crime-solving tool. FBI Law Enforcement Bulletin

Ivanchenko VN, Incerti S, Francis Z, Tran HN, Karamitros M, Bernal MA, Champion C, Guèye P (2012) Combination of electromagnetic physics for microdosimetry in liquid water with the Geant4 Monte Carlo simulation toolkit. Nucl Instrum Methods Phys Res B 273:95–97

Jarry G, DeMarco JJ, Beifuss U, Cagnon CH, McNitt-Gray MF (2003) A Monte Carlo-based method to estimate radiation dose from spiral CT: from phantom testing to patient-specific models. Phys Med Biol 48(16):2645–2663

Kanias T, Acker JP (2006) Mammalian cell desiccation: facing the challenges. Cell Preserv Technol 4:253–277

Kefi R (2011) Ancient DNA investigations: a review on their significance in different research fields. Int J Anthrop 4:61–76

Keller G, Hoffmann B (2000) The radon diffusion length as a criterion for the radon tightness. In: IRPA10 conference proceedings, Hiroshima

Kellerer AM (1980) Biophysikalische Grundlagen der Medizin, Beiträge zur Theorienbildung. Gustav Fischer Verlag, Stuttgart

Kim S, Song H, Samei E, Yin FF, Yoshizumi TT (2011) Computed tomography dose index and dose length product for cone-beam CT: Monte Carlo simulations. J Appl Clin Med Phys 12(2):3395

Knapp M, Hofreiter M (2010) Next generation sequencing of ancient DNA: requirements, strategies and perspectives. Genes 1:227–243

Koenig W (1896) 14 Photographien von Roentgen-Strahlen aufgenommen im Physikalischen Verein zu Frankfurt a. M. JA Barth, Leipzig

Kudryashov YB (2008) Radiation biophysics (ionizing radiation). Nova Sci, New York

Lea DE (1955) Actions of radiations on living cells, 2nd edn. Cambridge University Press, New York

Lynnerup N (2007) Mummies. Yearb Phys Anthropol 50:162–190

Meyer P, Groetz JE, Katz R, Fromm M, Chambaudet AM (1997) Simulation of a microdosimetry problem: behaviour of a pseudorandom series at a low probability. J Chem Soc, Cambridge, pp 282–285

Mullis K, Fallona FA (1987) Specific synthesis of DNA in vitro via a polymerase-catalyzed chain reaction. Meth Enzym 155:335–350

Öhrström L, Bitzer A, Walther M, Rühli FJ (2010) Technical note: Terahertz imaging of ancient mummies and bone. Am J Phys Anthropol 142(3):497–500

Okada S (1970) In: Altman K, Gerber G, Okada S (eds) Radiation biochemistry, vol 1. Academic, New York

Parson W (2009) Bedeutung der mtDNA-Analyse für forensische Fragestellungen. Springer, Medizin Verlag. http://link.springer.com/content/pdf/10.1007%2Fs00194-009-0594-3.pdf#page-1. Accessed 5 Feb 2013

Physics Reference Manual (2010) Version: Geant4 9.4

Poinar HN, Schwarz C, Qi J, Shapiro B, Macphee RD, Buiques B, Tikhonov A et al (2006) Metagenomics to paleogenomics: large-scale sequencing of mammoth DNA. Science 311(5759):392–394

Roots R, Okada S (1972) Protection of DNA molecules of cultured mammalian cells from radiation-induced single-strand scissions by various alcohols and SH compounds. Int J Radiat Biol 21:329–342

Rossi HH, Zaider M (1996) Microdosimetry and its applications. Springer, Heidelberg

Rühli F, von Waldburg H, Nielles-Vallespin S, Böni T, Speier P (2007) Clinical magnetic resonance imaging of ancient dry mummies without rehydration. JAMA 298:2618–2620

Saber-Khiabani E (2012) Mitochondrial DNA. http://de.scribd.com/doc/91405619/mito-dna. Accessed 3 Oct 2012

Semikhodskii A (2007) Dealing with DNA evidence a legal guide. Routledge-Cavendish, London

Unnik JGV, Broerse JJ, Geleijns J, Jansen JThM, Zoetelief J, Zweers D (1997) Survey of CT techniques and absorbed dose in various Dutch hospitals. Brit J Radiol 70:367–371

UNSCEAR (2010) Sources and effects of ionizing radiation: UNSCEAR 2008 Report to the General Assembly, with Scientific Indexes: UN

Wang ZM, Shen W, Kotler DP, Heshka S, Wielopolski L, Aloia JF, Nelson ME, Pierson RN Jr, Heymsfield SB (2003) Total-body protein: a new cellular mass and distribution prediction model. Am J Clin Nutr 78:979–984

Wilson DE (1959) The effect of ionizing radiation on the enzyme desoxyribonuclease in the dry state. Int J Rad Biol 4:360–365

Xun J, Hao Y, Xuejun G, Steve BJ (2012) Fast Monte Carlo simulation for patient-specific CT/CBCT imaging dose calculation. Phys Med Biol 57:577

Zaidi H, Ay MR (2007) Current status and new horizons in Monte Carlo simulation of X-ray CT scanners. Med Biol Eng Comput 45(9):809–17